Received: 11 December 2024 | Accepted: 18 March 2025

DOI: 10.1002/mgea.70010

RESEARCH ARTICLE

MGE ADVANCES
Materials Genome Engineering

High throughput characterization method of electrical and phonon properties by dielectric resonant spectroscopy

Ziru Wang[1,2] | **Mingyang Qin**[2] | **Peng Zhang**[3] | **Yiguo Xu**[3] | **Shiting Que**[2] | **Feng Yan**[1] | **X.-D. Xiang**[3,4,5]

[1]Department of Applied Physics, The Hong Kong Polytechnic University, Hong Kong SAR, China

[2]Department of Materials Science and Engineering, Southern University of Science and Technology, Shenzhen, China

[3]Academy for Advanced Interdisciplinary Studies, Southern University of Science and Technology, Shenzhen, China

[4]Songshan Lake Materials Laboratory, Dongguan, China

[5]Department of Physics, Southern University of Science and Technology, Shenzhen, China

Correspondence

Peng Zhang, Feng Yan and X.-D. Xiang.
Email: zhangp3@sustech.edu.cn, apafyan@polyu.edu.hk and xiangxd@sustech.edu.cn

Abstract

With the advancement of Materials Genome Initiative, there is an urgent need for nondestructive, rapid characterization methods for obtaining electrical transport properties and phonon information of materials. In this article, we develop a method using the dielectric resonant spectroscopies of materials to derive critical parameters such as conduction electron frequency, quantum relaxation time, and phonon frequency for metals and semiconductors. As a typical example, based on the new approaches, we realized simultaneous extraction of carrier concentration n and electron-phonon relaxation time τ_{e-p}, and establish a new relationship of $\tau_{e-p} = C^* \cdot T^{-1} \cdot n^{-1/3}$ for n-type doped silicon, where the true electron-phonon coupling constant C^* is proposed for the first time. This innovative methodology offers significant potential for high-throughput screening of materials, expediting the development of next-generation electronic devices.

KEYWORDS

dielectric resonant spectroscopy, high throughput characterization method, phonon properties, transport properties

1 | INTRODUCTION

"The Fourth Paradigm" of scientific research, as proposed by Jim Gray,[1] promotes the extraction of scientific knowledge from experimental data by artificial intelligence (AI). This has brought a revolutionary paradigm shift in materials science. However, the data-driven science relies heavily on the quantity and quality of data. Although AI has demonstrated great potential in materials science research,[2–4] the lack of experimental data in this field has hindered the successful implementation of this new paradigm. Recently, this issue has begun to be addressed by Materials Genome Initiative (MGI)[5] in which high-throughput experiments and computation are considered the means to generate data rapidly. "Data foundries"[5,6] are the critical infrastructures built to mass-produce large amounts of data systematically to meet the data demand.

Far-field photolithography technique played a critical role in ensuring the number of transistors in an integrated circuit (IC) chip grows according to Moore's law.[7] From past experiences, for AI approach to succeed in a field, it requires the relevant data to grow according to Moore's Law as in astrophysics[8] and biomedical fields.[9–13] Similar to the exponential growth rate observed in IC chip development under Moore's Law, far-field telescopes have catalyzed a comparable scaling trajectory in astrophysical data acquisition throughout modern observational astronomy. The optical probe technique and far-field optical microscopy played the same role in the development of gene sequence technology. They have demonstrated a significant value in managing the data surge in

Ziru Wang and Mingyang Qin contributed equally to this work.

gene sequencing and astrophysics, which has the potential to significantly enhance the efficiency of acquiring material data and advancing AI in materials science. Inspired by the above observations, we realized that the far-field optical methods to acquire physical properties of materials could be the key to breaking the bottleneck of materials data growth rate. To this end, new techniques of nondestructive (noncontact) and rapid material characterization with wavelength-limited spatial resolution are called for.

Electronic transport properties, serving as the fundamental physical characteristics of materials, play a significant role in characterizing the performance of thermoelectric, superconducting materials, and many other types of electronic devices. Among these electrical properties, free carrier density and relaxation time are essential parameters determining other critical electron transport metrics, such as resistivity and mobility. On the other hand, the phonon information is essential to understanding the mechanical properties of materials and the electron-phonon coupling phenomena.[14,15] Efficiently measuring and accurately extracting the aforementioned information is essential for a deeper understanding of electronic transport properties and the development of next-generation electronic materials.

Traditionally electrical conductivity (σ, is proportional to the electron-phonon relaxation time τ_{e-p} for metal behavior) is measured by the 4-point contact method (see Figure 1a), whereas the carrier density n is determined via the Hall effect, requiring additional transverse contacts with different geometries (see Figure 1b). However, due to uncertainties in sample geometry and the challenges associated with measurements on samples with low carrier density, it is difficult to determine $\tau_{e-p} - n$ dependency accurately in a wide range to obtain the scaling power law for n dependency. This has clouded the determination of true electron-phonon coupling constant in the past.

Fortunately, the electron or phonon interacting with the light field is uniquely represented in the spectrum, which provides us with the opportunity to extract relevant information. In the realm of optical measurements of electron transport properties, Drude proposed a simple model in 1900 to describe the dynamics of electrons in metals under the influence of an external electric field.[16] This model was later refined by Sommerfeld and others[17,18] by incorporating quantum theory, resulting in the Drude–Sommerfeld model, which can be applied to all conductive materials with free-likely electrons. According to the Drude–Sommerfeld model, optical conductivity can be expressed as[18]

$$\sigma(\omega) = \sigma_r(\omega) + i \cdot \sigma_i(\omega) = \frac{\omega_p^2 \tau_D}{4\pi} \frac{1 + i \cdot \omega\tau_D}{1 + \omega^2 \tau_D^2} \quad (1)$$

where $\omega_p = \left(\frac{4\pi n e^2}{m^*}\right)^{1/2}$ is the plasma frequency, n is the free carrier density, m^* is the effective mass, and τ_D is the Drude

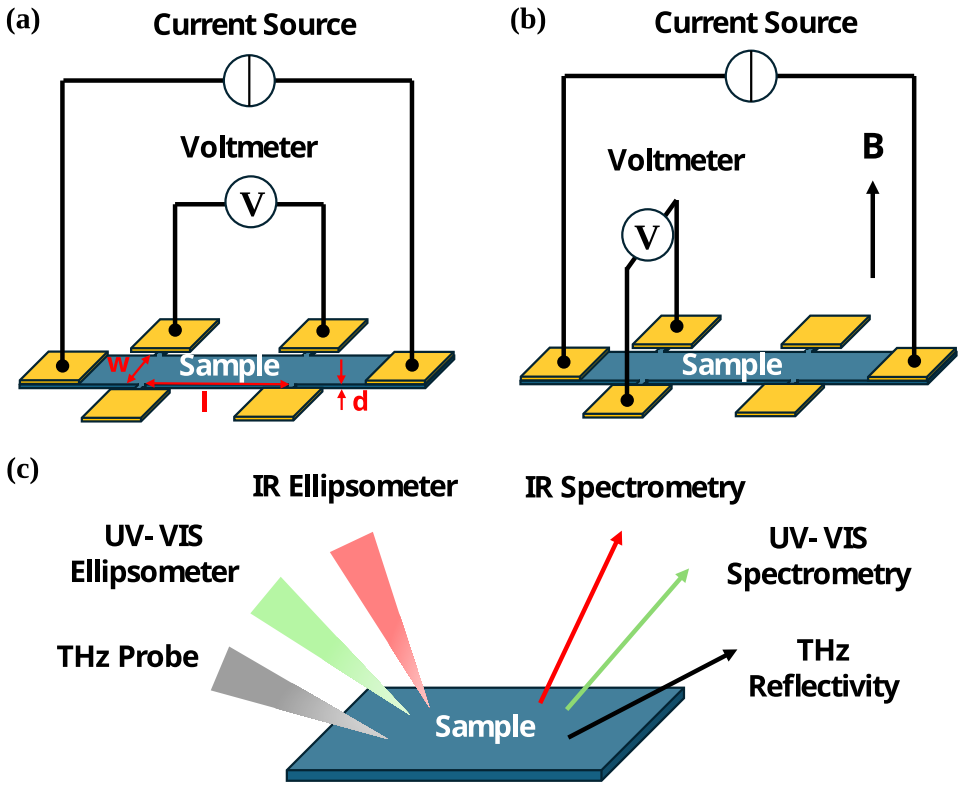

FIGURE 1 (a) Schematic of the four-probe contact method experimental setup, where w, l, and d are the width, length, and height of the sample, respectively. (b) Schematic of the Hall measurement contact method experimental setup. (c) Schematic of the noncontact dielectric resonant spectroscopy experimental setup.

quantum relaxation time, which is the same as the conventional DC electrical measurement as Drude assumed. From the general relation $\varepsilon(\omega) = \varepsilon_r(\omega) + i \cdot \varepsilon_i(\omega) = \left[1 - \frac{4\pi}{\omega}\sigma_i(\omega)\right] + i \cdot \frac{4\pi}{\omega}\sigma_r(\omega)$, the dynamics of free carriers can be characterized by dielectric functions[18]:

$$\varepsilon^D(\omega) = \varepsilon_r^D(\omega) + i \cdot \varepsilon_i^D(\omega) = 1 - \frac{\omega_p^2}{\omega^2 + \tau_D^{-2}} + i \cdot \frac{\omega_p^2}{\omega\tau_D\left(\omega^2 + \tau_D^{-2}\right)} \quad (2)$$

A typical dielectric spectrum of potassium based on the Drude–Sommerfeld model is shown in Figure 2a. At plasma resonance, $\varepsilon_r(\omega)$ becomes zero and $\varepsilon_i(\omega)$ exhibits a smooth variation, which is insufficient to capture the peak characteristics of free electron resonance. In contrast, dielectric loss function (DLF) $1/\varepsilon(\omega)$[18] can effectively highlight the plasma resonance. As depicted in Figure 2b, a resonant peak is observed at the plasma frequency ω_p in a dielectric loss image.

DLF has been employed to optically obtain relaxation time and carrier density for various metals.[19–22] However, the results based on Drude parameters often show significant deviations from experimental ones (see Figure 2b,d).[19] As noted in our previous research,[19] both $\varepsilon^D(\omega)$, arising from the response of conduction electrons as described by the Drude model, and $\varepsilon^B(\omega) = \varepsilon_r^B(\omega) + i \cdot \varepsilon_i^B(\omega)$, arising from the polarization response of bound electrons, should be included in new DLF-BE analysis as $\varepsilon(\omega) = \varepsilon^D(\omega) + \varepsilon^B(\omega)$ under the influence of electromagnetic fields:

$$\mathrm{Re}\left\{\frac{1}{\varepsilon(\omega)}\right\} = \frac{1 - \frac{\omega_p^2}{\omega^2 + \tau_D^{-2}} + \varepsilon_r^B(\omega)}{\left[1 - \frac{\omega_p^2}{\omega^2 + \tau_D^{-2}} + \varepsilon_r^B(\omega)\right]^2 + \left[\frac{\omega_p^2}{\omega\tau_D\left(\omega^2 + \tau_D^{-2}\right)} + \varepsilon_i^B(\omega)\right]^2} \quad (3)$$

and

$$-\mathrm{Im}\left\{\frac{1}{\varepsilon(\omega)}\right\} = \frac{\frac{\omega_p^2}{\omega\tau_D\left(\omega^2 + \tau_D^{-2}\right)} + \varepsilon_i^B(\omega)}{\left[1 - \frac{\omega_p^2}{\omega^2 + \tau_D^{-2}} + \varepsilon_r^B(\omega)\right]^2 + \left[\frac{\omega_p^2}{\omega\tau_D\left(\omega^2 + \tau_D^{-2}\right)} + \varepsilon_i^B(\omega)\right]^2}. \quad (4)$$

The new DLF-BE analysis demonstrated two main effects[19]: first one is the screening effect, resulting from the

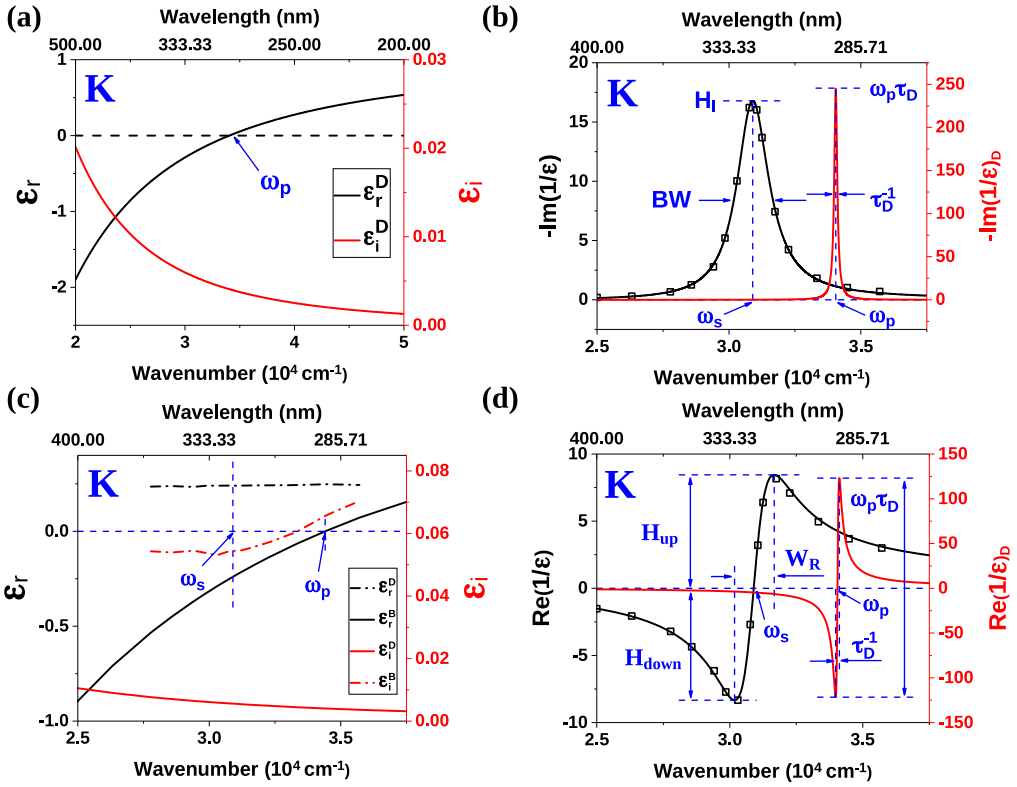

FIGURE 2 Optical analysis of potassium. (a) Real and imaginary parts of the frequency dependent dielectric function of the Drude model for $\omega_p = 34,048\ \mathrm{cm}^{-1}$ and $\tau_D^{-1} = 139\ \mathrm{cm}^{-1}$. (b, d) Imaginary and real parts of the dielectric loss function, where the Drude model, DLF-BE model[19], and experimental data[20] are represented by the red line, black line, and black dots, respectively. (c) Comparison of dielectric function contributions from the Drude term $\varepsilon^D(\omega)$ and the bound-electron term $\varepsilon^B(\omega)$, where the bound term, obtained as $\varepsilon^B(\omega) = \varepsilon(\omega) - \varepsilon^D(\omega)$, is shown as a dash-dot line. All the fitting parameters are consistent with those in ref 19.

real part of the bound electron dielectric constant ε_r^B, and it causes a shift from the bare plasma frequency ω_p to the screened plasma frequency ω_s:

$$\omega_s^2 = \frac{\omega_p^2}{1+\varepsilon_r^B(\omega_s)} - \tau_D^{-2} \tag{5}$$

Second one is the inelastic scattering effect between conduction and bound electrons, showing a broadening of the resonance peak through an additional scattering term:

$$\tau_{\mathrm{AC}}^{-1}(\omega_s) = \frac{\varepsilon_i^B(\omega_s)\omega_s}{1+\varepsilon_r^B(\omega_s)}. \tag{6}$$

Ignoring the second contribution leads to large discrepancies between the Drude model and experimental data[19] as shown in Figure 2b,d. In Figure 2c, $\varepsilon_i^B(\omega)$ was significantly larger than $\varepsilon_i^D(\omega)$ around ω_s, illustrating that the bound electron contributions must be considered.

In this work, we present the high-throughput characterization methods of electrical transport and phonon properties using the dielectric resonant spectrum method (Figure 1c). When ellipsometry spectroscopy data were available, an improved method focusing on the data within the bandwidth (BW) of DLF was introduced to extract the transport properties. In cases where optical phonon resonant frequency approaches the conduction electron plasma resonant, a single oscillator phonon resonant model was incorporated into the DLF analysis. For situations where only reflectance data over the plasma resonance are available, the reflectance spectrum was directly fitted with Drude and the phonon model was supplemented by bound electron contributions as the accurate constraint between real and imaginary parts of complex dielectric constant. To illustrate the applicability of these methods, we demonstrate examples of extracting the electron-phonon scattering rate τ_{e-p}^{-1} for both metals and semiconductors. Utilizing the carrier density n and relaxation time τ_{e-p} acquired from optical characterization, the relationship $\tau_{e-p} = C^* \cdot T^{-1} \cdot n^{-1/3}$ was established and an electron-phonon coupling constant C^* was obtained for n-type doped silicon.

2 | TRANSPORT PROPERTIES MEASUREMENT BY PLASMA RESONANCE SPECTRUM

In our previous study, only the imaginary part of DLF analysis was employed, where a broad experimental spectrum is typically required, which challenges the assumption that $\varepsilon_r^B(\omega)$ and $\varepsilon_i^B(\omega)$ remain constant as frequency varies (see Figure 2c). We later recognized that by employing the analysis of the real part of the DLF, a much narrower frequency range is sufficient, and the assumption of constant $\varepsilon_r^B(\omega)$ and $\varepsilon_i^B(\omega)$ becomes more reasonable.

By examining the graphical features of both real and imaginary parts of DLF-BE (see Figure 2a,d), we identify four key features from $\mathrm{Re}\{1/\varepsilon(\omega)\}$ function: the height H, the asymmetric height H_A, the bandwidth W, and the effective plasma frequency ω_s. When $\omega_p\tau_D \gg 1$, these features can be analytically or numerically derived to be associated with four fundamental unknown parameters ω_p, τ_D, $\varepsilon_r^B(\omega)$, and $\varepsilon_i^B(\omega)$ as follows:

$$H = H_{\mathrm{up}} + H_{\mathrm{down}} = \frac{\omega_s}{1+\varepsilon_r^B(\omega_s)}\,\tau_o(\omega_s) \tag{7}$$

$$W = \frac{1}{\tau_o(\omega_s)} = \frac{1}{F}\cdot\frac{1}{\tau_D}, F = \frac{\tau_o(\omega_s)}{\tau_D} \tag{8}$$

$$H_A = H_{\mathrm{up}} - H_{\mathrm{down}} = \alpha(F)\cdot F \tag{9}$$

where H_{up} and H_{down} represent the absolute maximum and minimum value of $\mathrm{Re}\{1/\varepsilon(\omega)\}$, $\tau_o(\omega_s)$ is the total optical quantum relaxation time, and $\alpha(F)$ characterizes the slope of the $H_A - F$ line, as shown in Figure 3c. In the Drude model, H_A can be expressed as $H_A = 2 - \frac{2\omega_p^2}{(2\omega_p+\tau_D^{-1})(2\omega_p-\tau_D^{-1})}$. Notably, when incorporating $\varepsilon_r^B(\omega)$ but assuming $\varepsilon_i^B(\omega) = 0$, H_A can be derived as follows:

$$H_A = \frac{1}{1+\varepsilon_r^B(\omega)}\left[2 - \frac{\frac{2\omega_p^2}{1+\varepsilon_r^B(\omega)}}{\left(\frac{2\omega_p}{\sqrt{1+\varepsilon_r^B(\omega)}}+\tau_D^{-1}\right)\left(\frac{2\omega_p}{\sqrt{1+\varepsilon_r^B(\omega)}}-\tau_D^{-1}\right)}\right]. \tag{10}$$

And H_A approaches to $\frac{1.5}{1+\varepsilon_r^B(\omega)}$ with the assumption of $\omega_p\tau_D \gg 1$. Therefore, a reduction of the experimental H_A from $\frac{1.5}{1+\varepsilon_r^B(\omega)}$ will confirm the presence of $\varepsilon_i^B(\omega_s)$. As shown

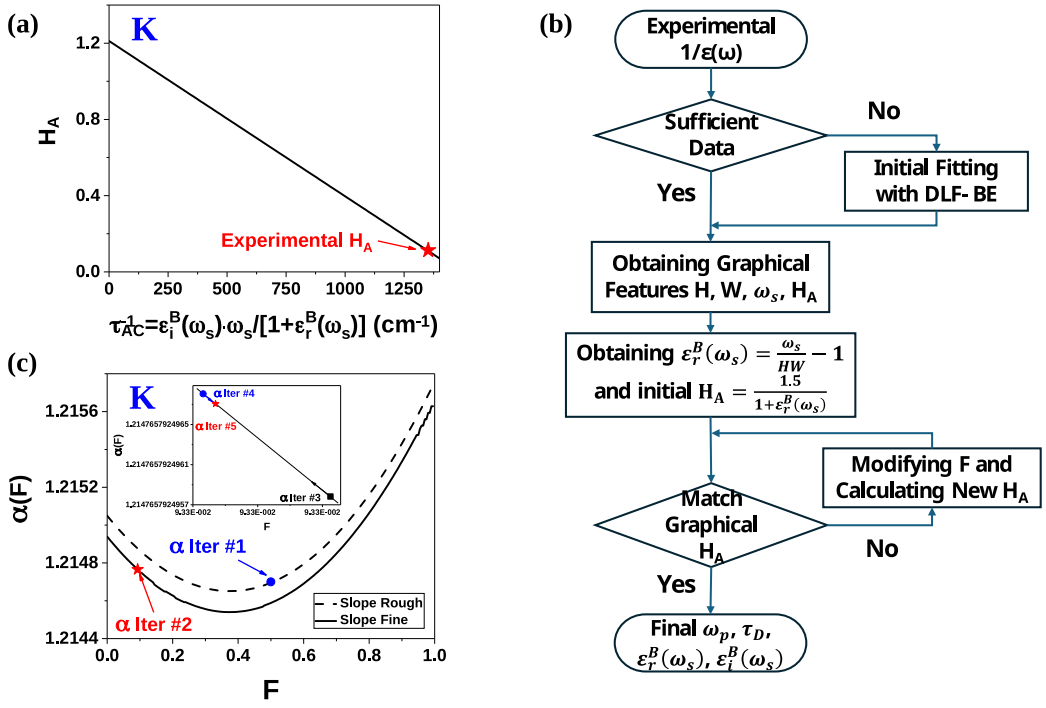

FIGURE 3 (a) Variation of H_A with respect to τ_{AC}^{-1} for potassium. The red star indicates the experimental value of H_A, which deviates significantly from H_A with $\varepsilon_i^B(\omega_s) = 0$ ($\tau_{AC}^{-1} = 0$). (b) Schematic of the iterative algorithm used to derive ω_p, τ_D, $\varepsilon_r^B(\omega_s)$, and $\varepsilon_i^B(\omega_s)$ from the graphical features H, W, ω_s, and H_A. (c) The relationship between the slope $\alpha(F)$ and F for potassium, illustrating the nonlinear dependence of H_A on F. The inset highlights the convergence of $\alpha(F)$ for potassium after five iterations.

in Figure 3a, the experimental H_A of potassium derived from the rough fitting curve is 0.1133, whereas H_A considering $\varepsilon_r^B(\omega_s)$ only is approximately 1.2, indicating that the influence of $\varepsilon_i^B(\omega_s)$ cannot be ignored in the dielectric loss spectrum. Furthermore, Equations (7)–(9) provide a means to solve for these four unknown parameters ω_p, τ_D, $\varepsilon_r^B(\omega)$, and $\varepsilon_i^B(\omega)$ as follows:

$$\tau_D = \frac{1}{W \cdot F} \tag{11}$$

$$\varepsilon_r^B(\omega_s) = \frac{\omega_s}{HW} - 1 \tag{12}$$

$$\varepsilon_i^B(\omega_s) = \frac{1 - F}{H} \tag{13}$$

$$\omega_p^2 = \left[\omega_s^2 + (W \cdot F)^2\right] \cdot \frac{\omega_s}{HW} \tag{14}$$

These equations demonstrate that $\tau_o(\omega_s)$ and $\varepsilon_r^B(\omega_s)$ can be directly solved from the graphical features. Once the parameter F is determined, the remaining three unknowns of τ_D, ω_p, and $\varepsilon_i^B(\omega_s)$ as well as the complete DLF can be fully resolved. Consequently, the uncertainties in τ_D, ω_p, and $\varepsilon_i^B(\omega_s)$ primarily depend on the accuracy of F.

The value of F could be determined through an iterative procedure as follows: initially, a value of F_{init} is selected and multiple H_A values are calculated by varying F within a specified range centered around F_{init}. Subsequently, $\alpha(F)$ is derived from the multiple calculated H_A values and their corresponding F. Using Equation (9), a new value of F is obtained based on this $\alpha(F)$ and the experimental $H_{A_{\text{exp}}}$. Next, H_A is recalculated in a narrower range around the updated F, yielding a corresponding new $\alpha(F)$. This iterative process continues until $\alpha(F)$ converges, resulting in an accurate determination of F and the corresponding τ_D, ω_p, and $\varepsilon_i^B(\omega_s)$. Combining Equations (11)–(14), the four unknowns $\varepsilon_r^B(\omega_s)$, τ_D, ω_p, and $\varepsilon_i^B(\omega_s)$ can be directly determined utilizing graphical features of the real component of DLF-BE. The iterative procedure is illustrated in Figure 3b, and a detailed schematic of the iteration steps for potassium is shown in Figure 3c. The diagram demonstrates that $\alpha(F)$ converges quickly within five steps, with an error of less than 1%.

To demonstrate the applicability of this method, we first examined the dielectric loss data of aluminum from which ω_p, τ_D, $\varepsilon_r^B(\omega)$, and $\varepsilon_i^B(\omega)$ were determined based on the graphical features of the real part of the DLF. The fitting results, shown in Figure 4a, reveal that the model closely aligns with the experimental data within the fitting range, with $R^2 = 0.998$ and 0.990 for the real and imaginary components of DLF-BE, respectively. The inset of Figure 4a demonstrates that α converged with less than 1% error (as indicated by Equation (9), the error in F is also below 1%), confirming that the graphical method itself introduces minor errors, well under 1%. Additionally, the fitting results of metal potassium, rubidium, and cesium were presented in

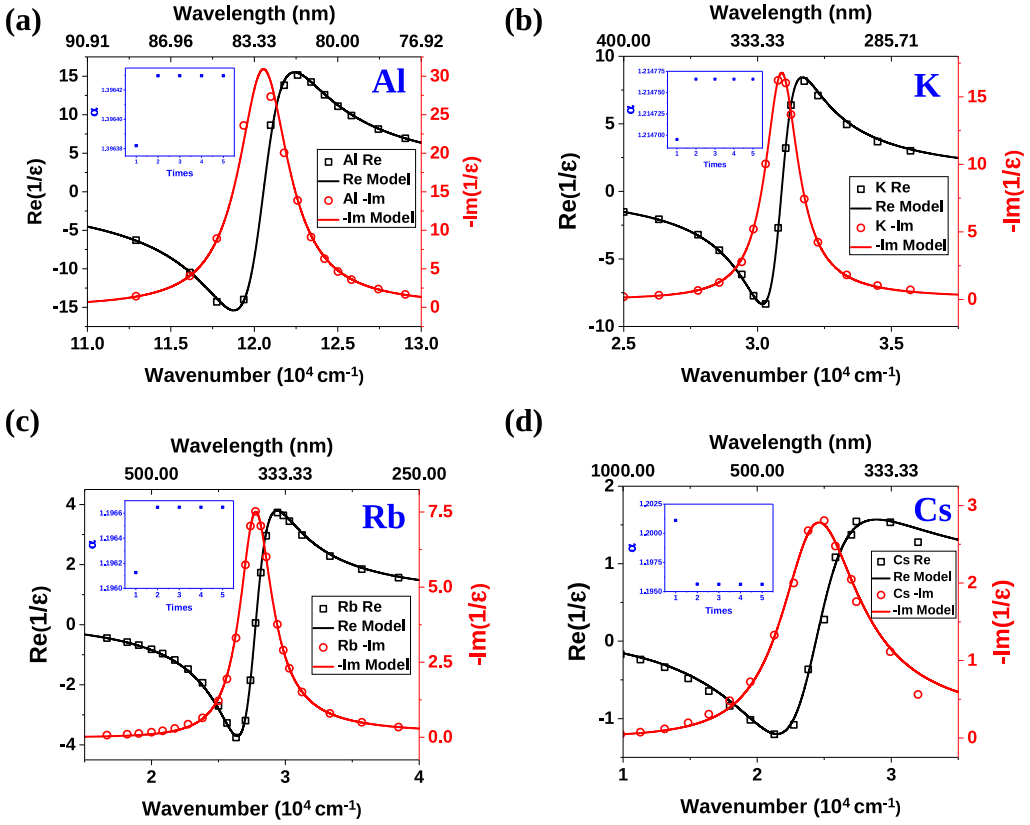

FIGURE 4 Fitting results for $\mathrm{Re}\{1/\varepsilon(\omega)\}$ and $-\mathrm{Im}\{1/\varepsilon(\omega)\}$ of (a) aluminum, (b) potassium, (c) rubidium, and (d) cesium at room temperature, along with the convergence of α for aluminum (inset of panel (a)), potassium (inset of panel (b)), rubidium (inset of panel (c)), and cesium (inset of panel (d)). In all cases, α converged within five iterations with a variation below 1%. Dielectric data for potassium, aluminum, rubidium, and cesium were obtained from refs. [20, 22–24], respectively.

Figure 4b–d, respectively, for reference. The R^2 values for the real and imaginary parts of DLF of K, Rb, and Cs were all above 0.985.

In ref. [19], the optical constants $n(\omega)$ and $\kappa(\omega)$ of aluminum[25] were fitted in the entire UV-VIS-IR spectrum by $\varepsilon(\omega) = \varepsilon^D(\omega) + \varepsilon^B(\omega)$, where $\varepsilon^B(\omega)$ was computed via density functional theory (DFT). The derived ω_p (106,873 cm^{-1}) was smaller than ω_s (121,007 cm^{-1}), which was qualitatively inconsistent with the fitting results for other metals: the screening effect reduced plasma resonant frequency ($\omega_s < \omega_p$). In contrast, our new analysis, which focuses exclusively on the dielectric loss data near the plasma resonance (with limited data within the BW), resulted in a ω_p (124,932 cm^{-1}) larger than ω_s (120,547 cm^{-1}). The derived τ_D^{-1} from graphical features was 260.0 cm^{-1}, which is smaller compared to the results (545 cm^{-1}) from ref. [19]. This discrepancy likely arises because the parameters are sensitive to fitting accuracy, and the graphical feature analysis provided a better fit near the plasma resonance. The plasma wavelength λ_p (calculated as $\lambda_p[\mathrm{nm}] = 10^7/\nu[\mathrm{cm}^{-1}]$) obtained from graphical features was ~80 nm, which, though smaller than the value obtained from DLF-BE (93 nm), was closer to the Drude results (79 nm).[26]

To further illustrate the practical application of this analysis, an examination of an indium-tin-oxide (ITO) film, a gallium-doped zinc oxide (GZO) film and two n-type silicon wafers were presented. Dielectric data for ITO and n-Si were obtained by the analysis of the amplitude ratio ψ and phase shift difference Δ between p- and s-polarized light waves at incident angles 55°, 65°, and 75°. These measurements were conducted by the M-2000 spectroscopic ellipsometer and the IR-VASE ellipsometer from J. A. Woollam in the VIS-UV range and the infrared region, respectively. The dielectric data of GZO were sourced from ref. [27]. Graphical features H, W, ω_s, and H_A of the real part of DLF at room temperature were extracted. From these features, the quantum relaxation time τ_D, the plasma frequency ω_p, and the elastic and inelastic bound electron contributions $\varepsilon_r^B(\omega_s)$ and $\varepsilon_i^B(\omega_s)$ were determined by iterating over α. It is crucial to emphasize that as ω_p and τ_D^{-1} converge, H should be measured directly as the value of $-\mathrm{Im}\{1/\varepsilon(\omega_s)\}$. Figure 5 demonstrates that the model, computed using parameters derived from these graphical features, is in good alignment with the experimental data for ITO, GZO, and n-Si, respectively. The insets of Figure 5 illustrate the convergence of α with respect to iteration steps, showing that the value of α converged after five iterations for

ITO, GZO, and n-Si, respectively, with all four achieving an error of less than 1%. Notably, in the original article,[27] the transport parameters of GZO were extracted by fitting the Drude model with a single oscillator to the ellipsometry data from 350 to 2000 nm, yielding ω_p and τ_D^{-1} values of 1.927 eV (15,542 cm^{-1}) and 0.117 eV (943.7 cm^{-1}), respectively. Our method, which relies solely on the graphical features of $\mathrm{Re}\{1/\varepsilon(\omega)\}$ within a much narrower range from 1120 to 1240 nm, produced similar results, with ω_p and τ_D^{-1} values of 15,471 and 833.8 cm^{-1}. By incorporating the contributions from inelastic bound electron with $\varepsilon_i^B(\omega) = 0.00167$, our results are expected to be more reliable.

Table 1 summarizes all parameters derived from the analysis of graphical features of $\mathrm{Re}\{1/\varepsilon(\omega)\}$. In four-point probe measurements, resistivity is calculated using $\rho = \frac{V}{I}\frac{dw}{l}$ (see Figure 1a) or from sheet resistance as $\rho = R_s d$, both of which introduce geometric uncertainties. Consequently, minor discrepancies between resistivity values obtained from optical and contact measurements are expected. For instance,

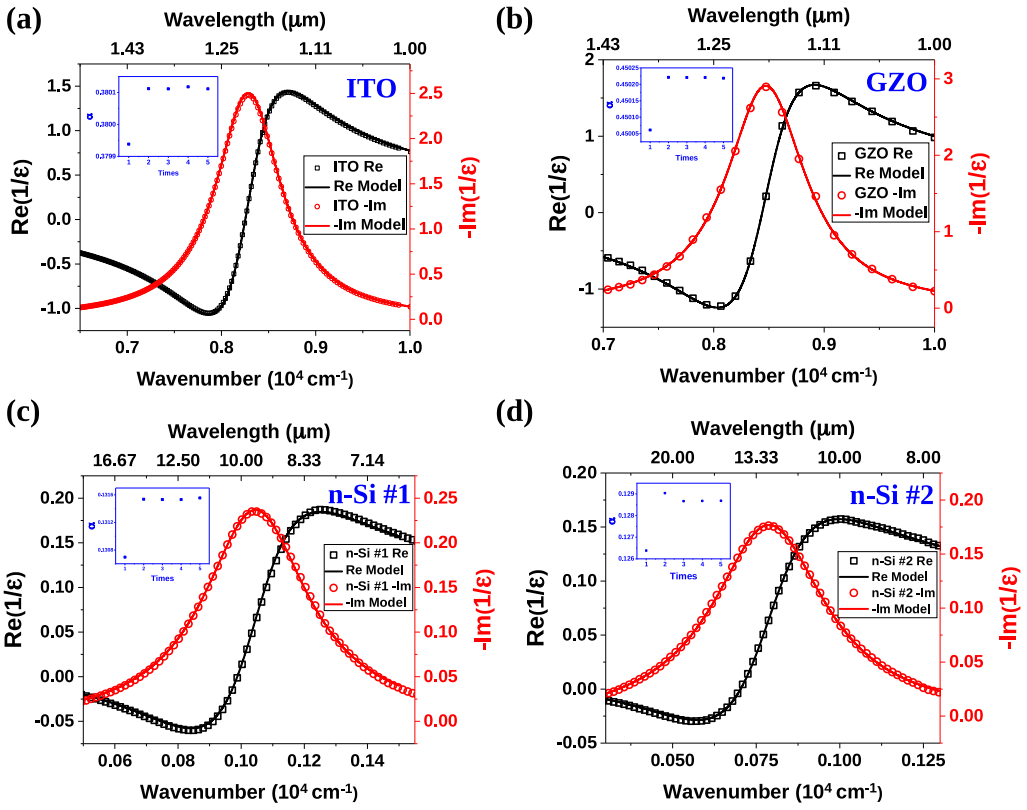

FIGURE 5 Fitting results for $\mathrm{Re}\{1/\varepsilon(\omega)\}$ and $-\mathrm{Im}\{1/\varepsilon(\omega)\}$ of the indium-tin-oxide film (a), the gallium-doped zinc oxide film (b), n-Si sample 1 (c), and sample 2 (d) at room temperature; Insets show the corresponding convergence of α. The R^2 values for the real and imaginary parts of DLF in panels (a–d) are all exceed 0.999.

TABLE 1 Fitting parameters obtained from the graphical feature method.

Materials	$\varepsilon_r^B(\omega_s)$	$\varepsilon_i^B(\omega_s)$	ω_p $(\mathbf{cm}^{-1})$	τ_D^{-1} $(\mathbf{cm}^{-1})$	τ_{AC}^{-1} $(\mathbf{cm}^{-1})$	F
Al	0.074	0.030	124,932	260.0	3370.7	0.0716
K	0.235	0.054	34,331	139.1	1352.2	0.0933
Rb	0.252	0.124	31,086	202.1	2752.5	0.0684
Cs	0.236	0.249	27,209	2200.4	4920.0	0.3077
ITO film	2.943	0.0035	16,470	834.1	7.42	0.9912
GZO film	2.328	0.0167	15,471	833.8	42.34	0.9517
n-Si #1	10.243	0.160	3557.8	387.8	14.06	0.9650
n-Si #2	10.393	0.0048	2747.3	409.9	0.294	0.9999

Abbreviations: GZO, gallium-doped zinc oxide; ITO, indium-tin-oxide.

the optically derived resistivities for potassium and rubidium, calculated using $\rho_{dc} = \frac{4\pi\tau_D^{-1}}{\omega_p^2}$, are 7.07 and 12.5 μΩ·cm, respectively, compared to four-probe measurement results of 7.20 and 12.8 μΩ·cm,[23] corresponding to errors of 1.8% and 2.4%. For the ITO film sample, the optically derived resistivity is 184 μΩ·cm, which falls well within the vendor-specified range of 170–200 μΩ·cm, demonstrating good consistency. Since the optical method is independent of sample geometry, resistivity obtained from resonance spectra is expected to be more reliable.

To provide a comprehensive understanding of the influence of $\varepsilon_i^B(\omega)$ on H_A, the relationships between $H_A \cdot \left[1 + \varepsilon_r^B(\omega_s)\right]$ and τ_{AC}^{-1} for metallic and semiconducting materials are shown in Figure 6a. Additionally, Figure 6b illustrates the relationship between $H_A \cdot \left[1 + \varepsilon_r^B(\omega_s)\right]$ and their corresponding final converged F. Notably, the results highlight that in metals, inelastic scattering by bound electrons is the dominant mechanism influencing the plasma resonant behavior of conduction electrons, whereas in semiconductors, although elastic scattering predominates, the contribution of $\varepsilon_i^B(\omega)$ should not be neglected. Figure 6a, b further demonstrate that H_A serves as a direct indicator of the presence of $\varepsilon_i^B(\omega)$.

3 | PHONON RESONANCE FEATURES IN DIELECTRIC SPECTRUM

Typically, the phonon resonance frequencies are obtained using the Raman or Brillouin scattering spectrometer. We here show that the phonon resonance features could be observed in the dielectric spectrum, which provides a high-throughput approach to simultaneously measure electron and phonon properties with the far-field optical probe. When the optical phonon frequency is close to the screened plasma frequency, the influence of bound electrons on conduction electrons around the screened plasma frequency deviates from constancy. This effect requires a more sophisticated model to accurately describe the dielectric behavior near the plasma frequency.

To model this interaction, a four-parameter semi-quantum model[26,28–30] defined as

$$\varepsilon^{\mathrm{ph}}(\omega) = \varepsilon_r^{\mathrm{ph}}(\omega) + i \cdot \varepsilon_i^{\mathrm{ph}}(\omega) = \left[1 + \varepsilon_r^B(\omega)\right] \frac{\left(\Omega_{\mathrm{LO}}^2 - \omega^2\right) + i \cdot \Gamma_{\mathrm{LO}}\omega}{\left(\Omega_{\mathrm{TO}}^2 - \omega^2\right) + i \cdot \Gamma_{\mathrm{TO}}\omega} \tag{15}$$

is incorporated into the dielectric function to approximate its behavior. In this equation, Ω_{LO} and Ω_{TO} represent the longitudinal optical (LO) and transverse optical (TO) phonon resonance frequencies, respectively, whereas Γ_{LO} and Γ_{TO} denote their corresponding damping rates. This function simplifies to the classical single-oscillator model when $\Gamma_{\mathrm{LO}} = \Gamma_{\mathrm{TO}}$. The influence of this phonon behavior is incorporated into the real and imaginary parts of the DLF, yielding

$$\mathrm{Re}\left\{\frac{1}{\varepsilon(\omega)}\right\} = \frac{\varepsilon_r^D(\omega) + \varepsilon_r^{\mathrm{ph}}(\omega)}{\left(\varepsilon_r^D(\omega) + \varepsilon_r^{\mathrm{ph}}(\omega)\right)^2 + \left(\varepsilon_i^D(\omega) + \varepsilon_i^{\mathrm{ph}}(\omega) + \varepsilon_i^B(\omega)\right)^2} \tag{16}$$

and

$$-\mathrm{Im}\left\{\frac{1}{\varepsilon(\omega)}\right\} = \frac{\varepsilon_i^D(\omega) + \varepsilon_i^{\mathrm{ph}}(\omega) + \varepsilon_i^B(\omega)}{\left(\varepsilon_r^D(\omega) + \varepsilon_r^{\mathrm{ph}}(\omega)\right)^2 + \left(\varepsilon_i^D(\omega) + \varepsilon_i^{\mathrm{ph}}(\omega) + \varepsilon_i^B(\omega)\right)^2}. \tag{17}$$

A fitting algorithm, such as least squares fitting, can then be applied to experimental dielectric loss data based on Equations (16) and (17) to extract parameters such as the plasma frequency ω_p and relaxation time τ_D.

To demonstrate the practical application of this model, we analyzed the electron transport properties of Nb-doped $SrTiO_3$. The dielectric data of one n-type Nb:$SrTiO_3$ wafer were optically obtained through a commercially available ellipsometer IR-VASE from J. A. Woollam in the

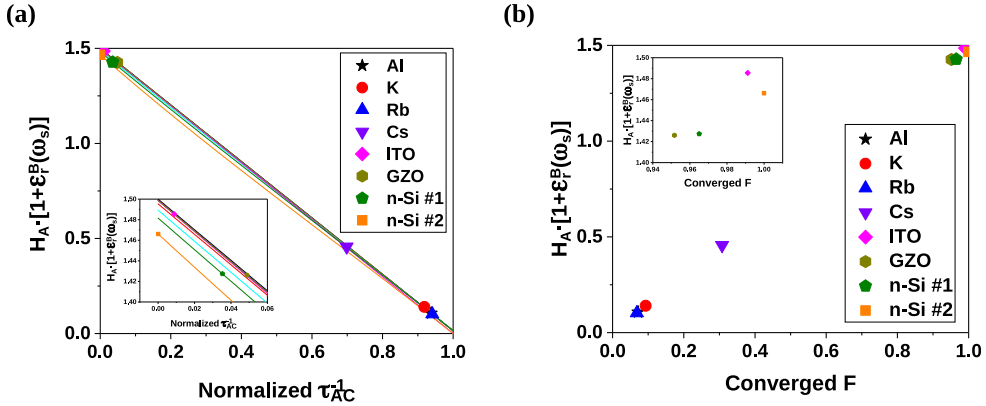

FIGURE 6 (a) The relationship between $H_A \cdot \left[1 + \varepsilon_r^B(\omega_s)\right]$ and normalized τ_{AC}^{-1} and (b) the relationship between $H_A \cdot \left[1 + \varepsilon_r^B(\omega_s)\right]$ and the corresponding final converged F for metals and semiconductors, based on the fitting results presented above. Insets in panels (a) and (b) provide detailed images for the semiconductors.

infrared region. DLF was subsequently calculated. Given the proximity of Ω_{TO} to the screened plasma frequency ω_s, the DLF model incorporating the phonon behavior, as outlined in Equations (16) and (17), was applied for fitting. Figure 7a presents the fitting results of the Nb:$SrTiO_3$ sample for the real component of the dielectric function and DLF over a broader range, whereas Figure 7b,c demonstrate the fitting results near Ω_{TO} and ω_s, respectively. An optical phonon was identified in the dielectric functions with a TO phonon frequency Ω_{TO} around 544.0 cm^{-1}, close to the previous reported value.[30] Meanwhile, an $\varepsilon_i^B(\omega)$ value of 0.22 was identified from the fitting, confirming that inelastic scattering must be considered even near phonon resonance.

A comparison of experimental data with individual fits using only phonon resonance model, or only Drude plasma resonance models, is presented in Figure 7e,f, respectively. In Figure 7c, the R^2 values for the fitting of real and imaginary parts of DLF over the frequency range shown are 0.9851 and 0.9794, respectively. Figure 7e shows that the single oscillator model for phonon alone could not adequately fit the experimental data around ω_0, with R^2 values of 0.9655 and 0.9852 for $\varepsilon_r(\omega)$ and $\varepsilon_i(\omega)$ only in the limited range of 500 to 600 cm^{-1}. The fitting parameters of considering both model contributions and only phonon or plasma resonance were summarized in Table 2. The negative ε_r^B value in the case of considering phonon only also indicated that plasma resonance effects cannot be neglected in this case. For the plasma resonance fitting, ω_p and τ_D^{-1} showed differences of +23.0% and +83.2%, respectively, between the cases of considering contributions from both models and the Drude model only. Therefore, for this Nb:STO sample, as demonstrated by Figure 7, analysis and extraction of physical parameters will not be accurate without considering the influence of both resonances.

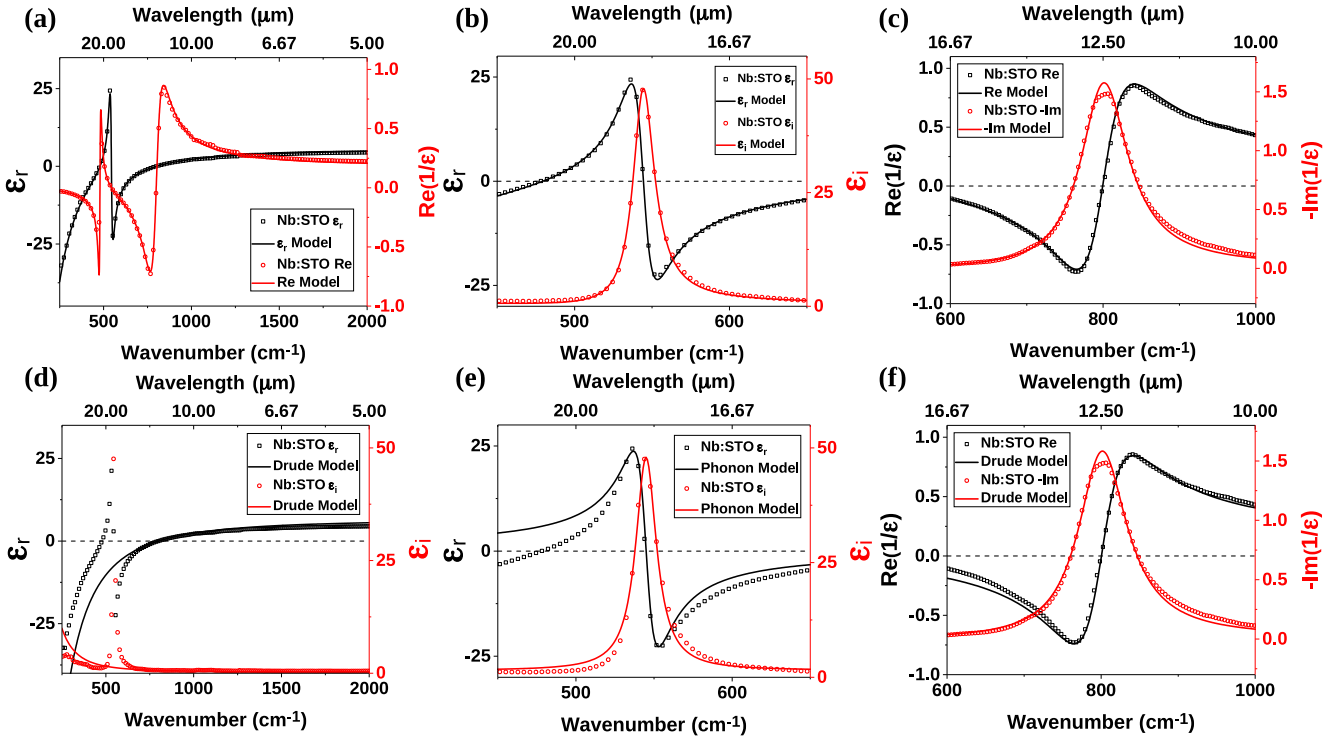

FIGURE 7 (a) Fitting results from Equations (16) and (17) for the real part of the dielectric function and dielectric loss function (DLF) of the STO sample over a broader spectral range, (b) near the phonon resonance presented in dielectric function, and (c) near the plasma resonance in DLF. (d) Comparison of experimental dielectric data of STO with fitting results from the Drude model alone over a wider range. (e) Fitting using the phonon model alone, focusing on the phonon resonance in the dielectric function. (f) Fitting using the Drude model alone around plasma resonance in the form of DLF. The experimental data presented in panels (a) and (d) have been resampled for clarity.

TABLE 2 Fitting parameters of the Nb-doped $SrTiO_3$ sample.

Model	ε_r^B	ε_i^B	Ω_{TO} (cm^{-1})	Γ_{TO} (cm^{-1})	Ω_{LO} (cm^{-1})	Γ_{LO} (cm^{-1})	ω_p (cm^{-1})	τ_D^{-1} (cm^{-1})	τ_{AC}^{-1} (cm^{-1})
Phonon + plasma	4.62 ± 0.1	0.22 ± 0.02	544.0 ± 0.1	16.8 ± 0.2	610.6 ± 0.7	36.6 ± 1.0	1672.1 ± 9.2	19.7 ± 3.9	38.1
Phonon only	−1.0	1.46	544.9	16.1	220,458	678,701	-	-	-
Plasma only	5.59	0.34	-	-	-	-	2057.2	36.1	-

4 | ANALYSIS FROM REFLECTANCE SPECTRUM

Terahertz (THz) technology, referring to the utilization of electromagnetic radiation in the frequency range between 0.1 and 10 THz, has garnered significant research interest due to its unique and complex interactions with materials across physical, chemical, and biological systems.[31–33] Within this frequency range, THz time-domain spectroscopy (THz-TDS)[34] is commonly employed to investigate the fundamental properties of materials. For optically thin samples, THz time domain transmission spectroscopy is typically employed, as it allows for the determination of the complex refractive index by fitting the transmission function to the amplitudes and relative phases.[33,35,36] For optically thick samples, THz time domain reflection spectroscopy (THz-TDRS) is preferred. In THz-TDRS, misalignments between the sample surface and the reference mirror can significantly affect the relative phases, whereas the amplitude spectrum is less influenced.[37,38] Therefore, directly fitting the THz reflectance spectrum is a practical method for extracting parameters in the THz region.

When the reflectance spectrum was directly fitted with a proper dielectric model, the model itself provides an accurate constraint between the real and imaginary parts of complex dielectric constant. By constructing the corresponding optical model based on Snell's law and Fresnel equations according to the experimental setup, the target parameters can be extracted. In the case of fitting a reflectivity spectrum near plasma resonance, the dielectric functions, considering the Drude, bound and phonon resonance terms, are expressed as follows:

$$\varepsilon_r(\omega) = \left[1 + \varepsilon_r^B(\omega)\right] \frac{\left(\Omega_{\mathrm{LO}}^2 - \omega^2\right)\left(\Omega_{\mathrm{TO}}^2 - \omega^2\right) + \Gamma_{\mathrm{TO}}\Gamma_{\mathrm{LO}}\omega^2}{\left(\Omega_{\mathrm{TO}}^2 - \omega^2\right)^2 + \Gamma_{\mathrm{TO}}^2\omega^2} - \frac{\omega_p^2}{\omega^2 + \tau_D^{-2}} \tag{18}$$

$$\varepsilon_i(\omega) = \left[1 + \varepsilon_r^B(\omega)\right] \frac{\left(\Omega_{\mathrm{TO}}^2 - \omega^2\right)\Gamma_{\mathrm{LO}}\omega - \left(\Omega_{\mathrm{LO}}^2 - \omega^2\right)\Gamma_{\mathrm{TO}}\omega}{\left(\Omega_{\mathrm{TO}}^2 - \omega^2\right)^2 + \Gamma_{\mathrm{TO}}^2\omega^2} + \frac{\omega_p^2}{\omega\tau_D\left(\omega^2 + \tau_D^{-2}\right)} + \varepsilon_i^B(\omega). \tag{19}$$

To illustrate its application, the reflectance of an n-type silicon wafer in the terahertz region was analyzed. The reflectance of n-Si was measured by the Laser Quantum HASSP THz spectrometer with a gold mirror as the reference. The THz beam was incident on the sample at a 30° angle and the beam was polarized in-plane (p-polarization). The p-polarized reflectance R_P data were fitted with the dielectric function model defined in Equations (18) and (19), from which the model parameters τ_D, ω_p, $\varepsilon_r^B(\omega_s)$, and $\varepsilon_i^B(\omega_s)$ were extracted.

The fitting results were shown in Figure 8a with an R^2 value of 0.9969. Additionally, Figure 8b displays the relationship between the real and imaginary parts of the dielectric functions $\varepsilon_r(\omega)$ and $\varepsilon_i(\omega)$ of n-Si, where the solid curves correspond to different values of reflectance R and the dashed line represents the Drude relationship. The intersection between two lines shows the reflectance as the accurate constraint between real and imaginary parts of complex dielectric constant. The ω_p and τ_D^{-1} obtained from the THz reflectance measurements were 183.9 ± 0.7 and 38.9 ± 0.3 cm^{-1}, respectively, resulting in a DC resistivity of 0.069 Ω·cm, which is in good agreement with the reported range of 0.05–0.1 and consistent with previous THz-TDRS measurements of n-Si.[37,38] The inelastic scattering term $\varepsilon_i^B(\omega)$ obtained from the fitting is $\sim 2.83 \times 10^{-15}$ with a fitting error of 0.122, suggesting that $\varepsilon_i^B(\omega)$ is difficult to determine at low frequencies.

5 | ELECTRON-PHONON SCATTERING IN METALLIC AND SEMICONDUCTING MATERIALS

The electron scattering rate τ_D^{-1} obtained from optical characterizations consists of three primary components: electron-phonon scattering τ_{e-p}^{-1}, electron-impurity/defect scattering τ_{e-i}^{-1}, and electron-electron scattering τ_{e-e}^{-1}. In bulk pure metals, electron-phonon scattering is the dominant contributor to resistivity at room temperature, with the effects of impurities, defects, and the external surfaces of the conductor being negligible.[39] According to Matthiessen's rule and Ohm's law,[18,19] the impurity scattering rate for pure metallic materials can be derived from their residual resistivity (the resistivity as $T \to 0$ K) based on temperature-dependent resistivity data. In chemically doped semiconductors, the Coulomb potential introduced by ionized impurities primarily governs electron-impurity scattering. As described by Brooks and Herring,[40–42] the ionized impurity scattering rate τ_{e-i}^{-1} is proportional to $T^{-3/2}$. Given that electron-phonon scattering exhibits a distinctive temperature dependence above Debye temperature, the two scattering rates τ_{e-p}^{-1} and τ_{e-i}^{-1} can be decoupled through temperature-dependent measurements.

According to Matthiessen's rule and Ohm's law,[18,19] the resistivity of metallic materials can be expressed optically as follows:

$$\rho_{\mathrm{dc}}(T) = \frac{4\pi}{\omega_p^2\tau_D(T)} = \frac{4\pi}{\omega_p^2}\left(\frac{1}{\tau_{e-i}} + \frac{1}{\tau_{e-p}(T)}\right) \tag{20}$$

For aluminum, the residual resistivity is approximately 0.0001 μΩ·cm,[23] showing that the electron-impurity

scattering can be considered negligible. Consequently, the electron-phonon scattering rate τ_{e-p}^{-1} of Al is approximately equal to τ_D^{-1}, which is around 260.0 cm^{-1} at room temperature from the fitting results above.

For chemically doped semiconductors, in the limited temperature range of 300–450 K, the electron-phonon scattering rate τ_{e-p}^{-1}, including acoustic phonons and optical phonons contribution, has an approximately linear relation with temperature.[43–45] Therefore, τ_{e-p}^{-1} and τ_{e-i}^{-1} of semiconductors could be roughly obtained by fitting the scattering rate across the temperature range from 300 to 450 K through the equation given below:

$$\frac{1}{\tau_D(T)} = \frac{1}{\tau_{e-i}(T)} + \frac{1}{\tau_{e-p}(T)} = a \cdot T^{-\frac{3}{2}} + b \cdot T \qquad (21)$$

To obtain τ_D^{-1} at the elevating temperature for the ITO film, the DLFs between 300 and 400 K were measured by the same ellipsometer in the UV/VIS region. The data were fitted under the assumption that ω_p, $\varepsilon_r^B(\omega_s)$, and $\varepsilon_i^B(\omega_s)$ remained consistent with their values at RT. From the temperature-dependent τ_D^{-1} values, the electron-impurity scattering rate τ_{e-i}^{-1} and the electron-phonon scattering rate τ_{e-p}^{-1} were calculated using Equation (21). The fitting results of τ_D^{-1} versus T for the ITO film sample were presented in Figure 9a. The uncertainty of τ_{e-p}^{-1}, estimated from the 95% confidence interval for parameter b in ITO, which characterizes its temperature dependence, was approximately ±7.6%.

For n-type silicon, spectroscopic ellipsometry measurements were conducted in the temperature range of 333–453 K in approximately 40 K intervals. Corresponding dielectric functions were obtained, and the DLFs were subsequently calculated and fitted with the assumption that ω_p remains unchanged from its value at 293 K. τ_{e-p}^{-1} of the n-Si sample 1 and 2 were determined using Equation (21), with τ_D^{-1} as a function of temperature presented in Figure 9b,c. Similarly, the estimated uncertainties of τ_{e-p}^{-1} for n-Si sample 1 and 2 were ±31.8% and ±2.5%, respectively. As for n-Si sample 3, the impurity concentration is low enough (carrier density $n = 9.8 \times 10^{16}\ cm^{-3}$) that the impurity-electron scattering can be negligible, and we can assume that $\tau_{e-p}^{-1} \approx \tau_D^{-1}$.

By comparing the calculated electron-phonon scattering rate τ_{e-p}^{-1} with carrier density n at room temperature, we observed a nearly linear relationship of the form $\tau_{e-p} \propto n^{-1/3}$ in n-Si wafers, as shown in Figure 10. This

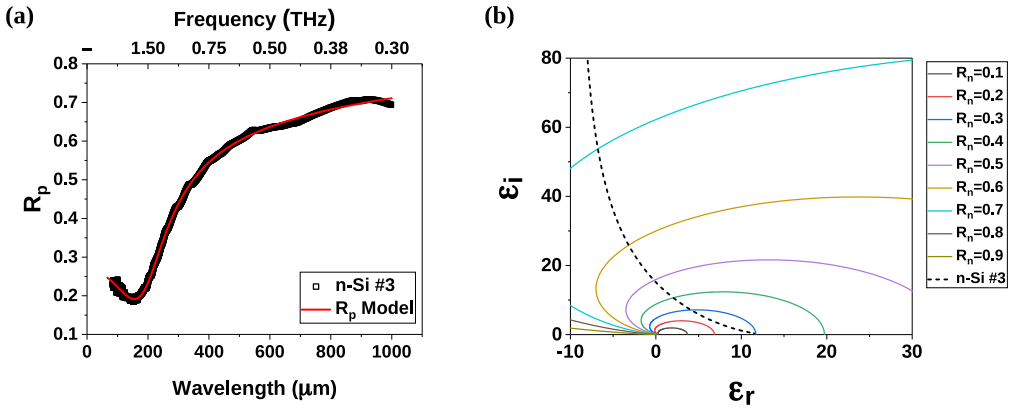

FIGURE 8 (a) Fitting results of the dielectric function $\varepsilon(\omega)$ incorporating both Drude and bound electron effects to the terahertz p-polarized reflectance R_p. (b) The relationship between $\varepsilon_r(\omega)$ and $\varepsilon_i(\omega)$ of the n-Si sample and their constrain with reflectance R.

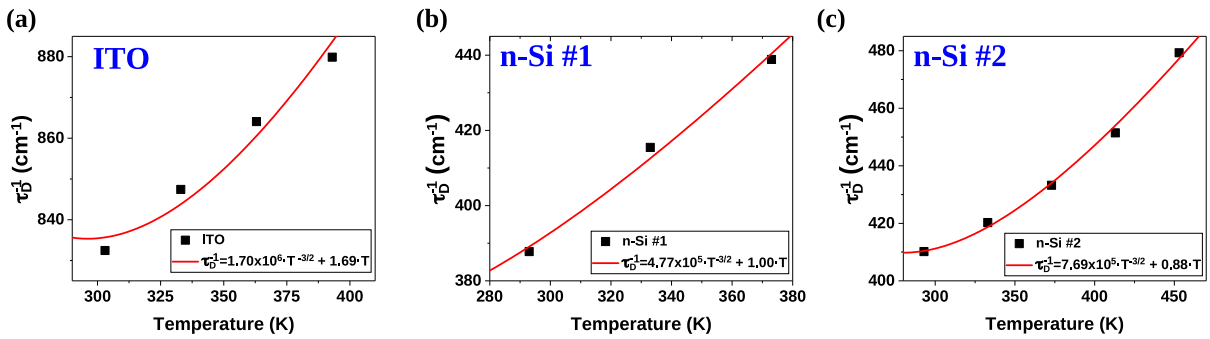

FIGURE 9 Temperature dependence of the electron scattering rate τ_D^{-1} for (a) the indium-tin-oxide film sample, (b) n-Si sample 1, and (c) n-Si sample 2, as calculated using Equation (21).

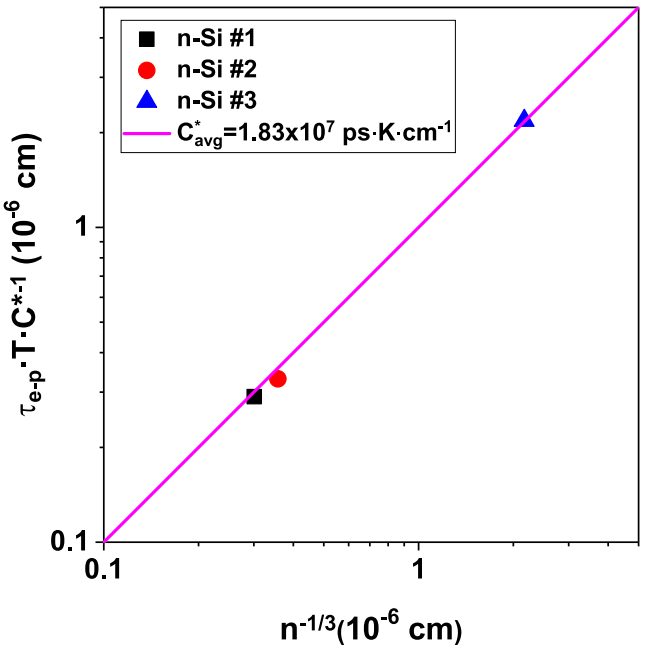

FIGURE 10 Linear fits of $\tau_{e-p} \cdot T \cdot C^{*-1}$ versus $n^{-1/3}$ for three n-Si samples at 293 K are presented. The weighted fitted C^* used in the calculations is 1.83×10^7 ps · K · cm^{-1}.

$\tau_{e-p} - n$ dependence contradicts the assumptions in the Migdal–Eliashberg model of superconductivity[46,47] and the Ioffe model of thermoelectricity,[48] both of which assume τ_{e-p} is independent of n. To further quantify this relationship, we define

$$\tau_{e-p} = C^* \cdot T^{-1} n^{-\frac{1}{3}}, \tag{22}$$

where C^* represents the electron-phonon coupling constant. A linear fit of $\tau_{e-p} \cdot T \cdot C^{*-1}$ against $n^{-1/3}$ of n-Si was presented in Figure 10, with $R^2 = 0.99$. Using optical fitting results from three differently doped n-type Si wafers, we determined the C^* for n-Si to be 1.83×10^7 ps · K · cm^{-1}, employing the weighted least squares method. The weights were computed based on the standard deviations of τ_{e-p}^{-1} for the three n-Si samples. The uncertainty of the C^*, estimated from the 95% confidence interval, was approximately ±0.9%. Additional sources of errors may stem from uncertainties in the effective mass of n-Si at room temperature. The effective mass utilized in these calculations was $0.26m_0$ for n-Si.[49]

6 | CONCLUSION

In this study, we demonstrate an enhanced optical method for determining key electrical and phonon parameters, including the electron scattering rate τ_D^{-1}, the plasma frequency ω_p, the elastic and inelastic bound electron dielectric components $\varepsilon_r^B(\omega_s)$ and $\varepsilon_i^B(\omega_s)$, and phonon resonance frequency from graphical features of the real part of the DLF $\mathrm{Re}\{1/\varepsilon(\omega)\}$. Additionally, we summarize the methods for determining the electron-phonon scattering rate τ_{e-p}^{-1} for both metallic and semiconducting materials, with examples from aluminum, ITO film, and n-type silicon wafers. Notably, a linear relationship $\tau_{e-p} = C^* \cdot T^{-1} \cdot n^{-1/3}$ was observed in n-type silicon and the electron-phonon coupling constant C^* was determined to be 1.83×10^7 ps · K · cm^{-1}. This novel finding challenges existing models in superconductivity and thermoelectricity and potentially paves the way for new theoretical frameworks in these fields.

AUTHOR CONTRIBUTIONS

X.-D.X. and P.Z. proposed and supervised the project. X.-D.X. and Y.X. developed and established the graphical feature method. Z.W. designed the experiments. Z.W. and S.Q. carried out the optical characterizations. Z.W. performed the data analysis. Z.W., P.Z., M.Q., F.Y., and X.-D. X. co-wrote the manuscript. All authors commented on the manuscript.

ACKNOWLEDGEMENTS

This work is supported by the Natural Science Foundation of China (12204220). This work was also supported by Shenzhen Basic Research Fund (Grant No. JCYJ20220818100612027, JCYJ20220530112816038). The authors thank Guangdong Provincial Key Laboratory of Sustainable Biomimetic Materials and Green Energy (2024B1212010003) and the Major Science and Technology Infrastructure Project of Material Genome Big-science Facilities Platform supported by the Municipal Development and Reform Commission of Shenzhen.

CONFLICT OF INTEREST STATEMENT

The authors declare no conflicts of interest.

DATA AVAILABILITY STATEMENT

The data that support the findings of this study are available from the corresponding author upon reasonable request.

ORCID

X.-D. Xiang https://orcid.org/0000-0002-6155-7713

REFERENCES

1. Nielsen M. The Fourth paradigm: data-intensive scientific discovery. *Nature*. 2009;462(7274):722-723.
2. Raccuglia P, Elbert KC, Adler PDF, et al. Machine-learning-assisted materials discovery using failed experiments. *Nature*. 2016;533(7601):73-76.
3. Jain A, Hautier G, Ong SP, Persson K. New opportunities for materials informatics: resources and data mining techniques for uncovering hidden relationships. *J Mater Res*. 2016;31(8):977-994.
4. Liu Y, Zhao T, Ju W, Shi S. Materials discovery and design using machine learning. *J Materiomics*. 2017;3(3):159-177.
5. Wang H, Xiang X-D, Zhang L. Data+ AI is the core of materials genomic engineering. *Sci Technol Rev*. 2018;36(14):15-21.
6. Wang H, Xiang X-D. On the data-driven materials innovation infrastructure. *Engineering*. 2020;6(6):609-611.

7. Schaller RR. Moore's law: past, present and future. *IEEE Spectrum*. 1997;34(6):52-59.
8. Council NR. *Astronomy and Astrophysics in the New Millennium: Panel Reports*. National Academies Press; 2001:400.
9. Mardis ER. A decade's perspective on DNA sequencing technology. *Nature*. 2011;470(7333):198-203.
10. Metzker ML. Sequencing technologies — the next generation. *Nat Rev Genet*. 2010;11(1):31-46.
11. Stein LD. The case for cloud computing in genome informatics. *Genome Biol*. 2010;11(5):207.
12. The human genome at ten. *Nature* 2010;464(7289):649-650.
13. Wetterstrand KA. *DNA Sequencing Costs: Data from the NHGRI Genome Sequencing Program (GSP)*. National Human Genome Research Institute; 2013.
14. Geerken BM, Griessen R, Huisman LM, Walker E. Contribution of optical phonons to the elastic moduli of PdH_x and PdD_x. *Phys Rev B* 1982;26(4):1637-1650.
15. Bouarissa N, Saib S. Elastic modulus, optical phonon modes and polaron properties in Al1−xBxN alloys. *Curr Appl Phys*. 2013;13(3):493-499.
16. Drude P. On the electron theory of metals. *Ann Phys*. 1900;1(3):566-613.
17. Sommerfeld A, Bethe H. Elektronentheorie der Metalle. In: *Aufbau Der Zusammenhängenden Materie*. Springer Berlin Heidelberg; 1933:333-622.
18. Dressel M, Grüner G. *Electrodynamics of Solids: Optical Properties of Electrons in Matter*. Cambridge University Press; 2002.
19. Zhang P, Tang H, Gu C, et al. A direct measurement method of quantum relaxation time. *Natl Sci Rev*. 2020;8(4).
20. Yamaguchi S, Hanyu T. Optical properties of potassium. *J Phys Soc Jpn*. 1971;31(5):1431-1441.
21. Yamaguchi S, Hanyu T. The optical properties of Rb. *J Phys Soc Jpn*. 1973;35(5):1371-1377.
22. Rakić AD. Algorithm for the determination of intrinsic optical constants of metal films: application to aluminum. *Appl Opt*. 1995;34(22):4755-4767.
23. Haynes WM, ed. *CRC Handbook of Chemistry and Physics*. 97th ed. CRC Press; 2016.
24. Smith NV. Optical constants of rubidium and cesium from 0.5 to 4.0 eV. *Phys Rev B*. 1970;2(8):2840-2848.
25. Marković M, Rakić A. Determination of optical properties of aluminium including electron reradiation in the Lorentz-Drude model. *Opt Laser Technol*. 1990;22(6):394-398.
26. Tanner DB. *Optical Effects in Solids*. Cambridge University Press; 2019.
27. Kim J, Naik GV, Emani NK, Guler U, Boltasseva A. Plasmonic resonances in nanostructured transparent conducting oxide films. *IEEE J Sel Top Quant Electron*. 2013;19(3):4601907.
28. Gervais F, Piriou B. Anharmonicity in several-polar-mode crystals: adjusting phonon self-energy of LO and TO modes in Al_2O_3 and TiO_2 to fit infrared reflectivity. *J Phys C Solid State Phys*. 1974;7(13):2374-2386.
29. Gervais, Fo, Servoin, JL, Baratoff, A, Bednorz, JG, Binnig, G. Temperature dependence of plasmons in Nb-doped $SrTiO_3$. *Phys Rev B* 1993;47(13):8187-8194,
30. Rubano A, Braun L, Wolf M, Kampfrath T. Mid-infrared time-domain ellipsometry: application to Nb-doped $SrTiO_3$. *Appl Phys Lett*. 2012;101(8):081103.
31. Shi Z-W, Cao X, Wen Q, et al. Terahertz modulators based on silicon nanotip array. *Adv Opt Mater*. 2018;6(2):1700620.
32. Ho L, Pepper M, Taday P. Signatures and fingerprints. *Nat Photonics*. 2008;2(9):541-543.
33. Jepsen PU, Cooke DG, Koch M. Terahertz spectroscopy and imaging – modern techniques and applications. *Laser Photon Rev*. 2011;5(1):124-166.
34. Grischkowsky D, Keiding S, van Exter M, Fattinger C. Far-infrared time-domain spectroscopy with terahertz beams of dielectrics and semiconductors. *J Opt Soc Am B*. 1990;7(10):2006-2015.
35. Duvillaret L, Garet F, Coutaz JL. A reliable method for extraction of material parameters in terahertz time-domain spectroscopy. *IEEE J Sel Top Quant Electron*. 1996;2(3):739-746.
36. Dorney TD, Baraniuk RG, Mittleman DM. Material parameter estimation with terahertz time-domain spectroscopy. *J Opt Soc Am A*. 2001;18(7):1562-1571.
37. Jeon T-I, Grischkowsky D. Characterization of optically dense, doped semiconductors by reflection THz time domain spectroscopy. *Appl Phys Lett*. 1998;72(23):3032-3034.
38. Nashima S, Morikawa O, Takata K, Hangyo M. Measurement of optical properties of highly doped silicon by terahertz time domain reflection spectroscopy. *Appl Phys Lett*. 2001;79(24):3923-3925.
39. Coffey KR. 9 – electron scattering in metallic thin films. In: Barmak K, Coffey K, eds. *Metallic Films for Electronic, Optical and Magnetic Applications*. Woodhead Publishing; 2014:422-453.
40. Brooks H. Theory of the electrical properties of germanium and silicon. In: Marton L, ed. *Advances in Electronics and Electron Physics*. Academic Press; 1955:85-182.
41. Herring C. Transport properties of a many-valley semiconductor. *Bell Syst Tech J*. 1955;34(2):237-290.
42. Peter Y, Cardona M. *Fundamentals of Semiconductors: Physics and Materials Properties*. Springer Science & Business Media; 2010.
43. Ma J, Nissimagoudar AS, Li W. First-principles study of electron and hole mobilities of Si and GaAs. *Phys Rev B*. 2018;97(4):045201.
44. Liu T-H, Zhou J, Liao B, Singh DJ, Chen G. First-principles mode-by-mode analysis for electron-phonon scattering channels and mean free path spectra in GaAs. *Phys Rev B*. 2017;95(7):075206.
45. Zhou J-J, Bernardi M. Ab initio electron mobility and polar phonon scattering in GaAs. *Phys Rev B*. 2016;94(20):201201.
46. Migdal A. Interaction between electrons and lattice vibrations in a normal metal. *Sov Phys JETP*. 1958;7(6):996-1001.
47. Eliashberg G. Interactions between electrons and lattice vibrations in a superconductor. *Sov Phys JETP*. 1960;11(3):696-702.
48. Ioffe AF, Stil'bans LS, Iordanishvili EK, Stavitskaya TS, Gelbtuch A, Vineyard G. Semiconductor thermoelements and thermoelectric cooling. *Phys Today*. 1959;12(5):42.
49. Horii H, Ueda A, Hayashi Y. Optimization of effective electron mass in strained silicon nanosheets. *AIP Adv*. 2024;14(1).

How to cite this article: Wang Z, Qin M, Zhang P, et al. High throughput characterization method of electrical and phonon properties by dielectric resonant spectroscopy. *Materials Genome Engineering Advances*. 2025;3(3):e70010. https://doi.org/10.1002/mgea.70010